Field-induced magnetic phase transitions and metastable states in Tb_3Ni

A. F. Gubkin,[1,2] L. S. Wu,[3] S. E. Nikitin,[4,5] A. V. Suslov,[6] A. Podlesnyak,[3] O. Prokhnenko,[7] K. Prokeš,[7] F. Yokaichiya,[7] L. Keller,[8] and N. V. Baranov[1,2,*]

[1]*M.N. Mikheev Institute of Metal Physics, Ural Branch of the Russian Academy of Sciences, 620108 Ekaterinburg, Russia*
[2]*Institute of Natural Sciences and Mathematics, Ural Federal University, 620083 Ekaterinburg, Russia*
[3]*Neutron Scattering Division, Oak Ridge National Laboratory, Oak Ridge, Tennessee 37831, USA*
[4]*Max Planck Institute for Chemical Physics of Solids, Nöthnitzer Strasse 40, 01187 Dresden, Germany*
[5]*Institut für Festkörper- und Materialphysik, Technische Universität Dresden, D-01069 Dresden, Germany*
[6]*National High Magnetic Field Laboratory, Tallahassee, Florida 32310, USA*
[7]*Helmholtz-Zentrum Berlin für Materialien und Energie, D-14109 Berlin, Germany*
[8]*Laboratory for Neutron Scattering and Imaging, Paul Scherrer Institut, 5232 Villigen PSI, Switzerland*

(Received 22 February 2018; revised manuscript received 11 April 2018; published 26 April 2018)

In this paper we report the detailed study of magnetic phase diagrams, low-temperature magnetic structures, and the magnetic field effect on the electrical resistivity of the binary intermetallic compound Tb_3Ni. The incommensurate magnetic structure of the spin-density-wave type described with magnetic superspace group $P112_1/a1'(ab0)0ss$ and propagation vector $\mathbf{k}_{IC} = [0.506,0.299,0]$ was found to emerge just below Néel temperature $T_N = 61$ K. Further cooling below 58 K results in the appearance of multicomponent magnetic states: (i) a combination of $\mathbf{k}_1 = [\frac{1}{2},\frac{1}{2},0]$ and $\mathbf{k}_{IC}$ in the temperature range $51 < T < 58$ K; (ii) a mixed magnetic state of $\mathbf{k}_{IC}$, $\mathbf{k}_1$, and $\mathbf{k}_2 = [\frac{1}{2},\frac{1}{4},0]$ with the partially locked-in incommensurate component in the temperature range $48 < T < 51$ K; and (iii) a low-temperature magnetic structure that is described by the intersection of two isotropy subgroups associated with the irreducible representations of two coupled primary order parameters (OPs) $\mathbf{k}_2 = [\frac{1}{2},\frac{1}{4},0]$ and $\mathbf{k}_3 = [\frac{1}{2},\frac{1}{3},0]$ and involves irreducible representations of the secondary OPs $\mathbf{k}_1 = [\frac{1}{2},\frac{1}{2},0]$ and $\mathbf{k}_4 = [\frac{1}{2},0,0]$ below 48 K. An external magnetic field suppresses the complex low-temperature antiferromagnetic states and induces metamagnetic transitions towards a forced ferromagnetic state that are accompanied by a substantial magnetoresistance effect due to the magnetic superzone effect. The forced ferromagnetic state induced after application of an external magnetic field along the *b* and *c* crystallographic axes was found to be irreversible below 3 and 8 K, respectively.

DOI: 10.1103/PhysRevB.97.134425

I. INTRODUCTION

Magnetic phase transitions are a matter of particular importance since they provide an insight into the fundamental physics of magnetic materials and determine their potential for use in technical applications. Evolution of magnetic and electronic properties of the rare-earth (R) transition-metal (T) intermetallic compounds as well as their interplay caused by magnetic phase transitions is still an attractive subject for fundamental science. An increasing demand for strong permanent magnets based on the R-T intermetallic compounds brought about a lot of research works focused on magnetic properties determined by an indirect $4f$-$3d$ exchange interaction of the Ruderman-Kittel-Kasuya-Yosida (RKKY) type. [1]. However, there is still much interesting basic science in the R-T intermetallic systems where the magnetic $4f$ electrons themselves as well as the indirect $4f$-$4f$ exchange interactions prevail and give rise to intriguing fundamental properties [2]. For instance, a strong coupling between localized $4f$ moments and the shape of the Fermi surface (FS) was found to determine the type of a magnetic order in pure rare-earth metals [3]. The decisive role of the FS geometry in explaining of the complex incommensurate magnetic orders in the ternary rare-earth silicides R_2PdSi_3 (R = Gd, Tb) and cerium hexaboride CeB_6 has been evidenced by means of magnetic neutron scattering and angle-resolved photoemission spectroscopy [4,5]. Recently, the enhanced short-range antiferromagnetic order persisting in Tb_3Ni and Gd_3Ni compounds up to five to six times the Néel temperature was found to originate from dominance of indirect $4f$-$5d$-$5d$-$4f$ exchange interaction between neighboring R ions over RKKY exchange [6].

Among the rare-earth intermetallic compounds, R_3T (T = Co, Ni) compounds possess the highest content of rare-earth metal within the binary R-T systems and exhibit a rich variety of physical properties: unconventional superconductivity [7,8], charge density wave [9], giant magnetoresistance effect [10,11], multicomponent magnetic structures exhibiting coexistence of commensurate and incommensurate propagation vectors [12,13], field-induced magnetic phase transitions [13–16], and giant magnetocaloric effect [17–20]. R_3T compounds crystallize in a low-symmetry orthorhombic structure of the Fe_3C type described with the space group $Pnma$ [21]. The rare-earth ions occupy two nonequivalent $4c$ and $8d$ Wyckoff positions with distances between neighboring R ions as short as in pure rare-earth metals (see Fig. 1 and

*Corresponding author: baranov@imp.uran.ru

 ©2018 American Physical Society

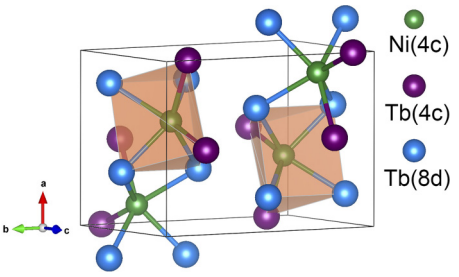

FIG. 1. Schematic visualization of the crystal structure of Tb_3Ni. Tb atoms located in 4*c* and 8*d* Wyckoff sites form distorted trigonal prisms enclosing Ni atoms located at 4*c* position.

Table I). The transition-metal ions are located at the 4*c* site inside the trigonal prisms formed by *R* ions and do not carry any magnetic moment [13,14,22], while spin fluctuations in 3*d* or 4*d* bands induced by *f*-*d* exchange may substantially affect macroscopic properties of the R_3T compounds [23]. In particular, spin fluctuations were suggested to be responsible for an enhanced value of the *T*-linear specific heat coefficient ($\gamma = 118\,\mathrm{mJ\,mol^{-1}\,K^{-2}}$ for Gd_3Rh [23] and $\gamma = 86\,\mathrm{mJ\,mol^{-1}\,K^{-2}}$ for Gd_3Ni [24]) as well as for the tendency to saturation of the electrical resistivity in the paramagnetic state [25,26]. The saturation of the resistivity observed in numerous R_3T compounds was also ascribed to the short-range magnetic order persisting up to temperatures well above Néel temperature and the *s*-*d* scattering mechanism [6,27]. The complex multicomponent incommensurate magnetic structures observed in R_3T with non-Kramers *R* ions apparently arise from the competition of exchange interactions of different types and low-symmetry crystal electric field [6,12–15].

Among the other R_3T compounds, Tb_3Ni is of particular interest since it exhibits several magnetic structure transformations on cooling below the Néel temperature $T_N = 61$ K [6]. Despite two neutron powder diffraction studies [6,14], the magnetic structure of this compound has not yet been fully established in detail. Due to the complex noncoplanar magnetic structures existing at low temperatures, the magnetization process reveals a rich variety of the field-induced magnetic phase transitions [14] that may substantially affect an anomalous behavior of the electrical resistivity observed on the polycrystalline Tb_3Ni sample [25]. If the magnetic phase diagram, low-temperature magnetic structures, and their interplay with electrical properties of the Tb_3Ni compound are to be clarified, measurements on single crystal samples are necessary.

TABLE I. Atomic coordinates and unit cell parameters at $T = 65$ K refined from our neutron powder diffraction data using orthorhombic space group *Pnma*.

Atoms	*x*	*y*	*z*
Ni(4*c*)	0.3918(5)	0.25	0.5531(6)
Tb(4*c*)	0.0309(7)	0.25	0.3562(9)
Tb(8*d*)	0.1800(5)	0.0651(3)	0.8209(7)

$a = 6.8342(3)$ Å, $b = 9.5262(4)$ Å, $c = 6.3306(3)$ Å
$\chi^2 = 2.8$, $R_B = 5.2\%$, $R_F = 4.2\%$

In this work, we present such a detailed study of the magnetic field effect. We report characterization of the low-temperature magnetic structures and magnetic phase diagrams of Tb_3Ni determined by means of magnetic and magnetoresistance measurements, single crystal neutron diffraction in high steady magnetic fields up to 180 kOe, and cold neutron powder diffraction below and above the Néel temperature.

II. EXPERIMENT

The Tb_3Ni ingot was prepared by induction melting of terbium and nickel metals in a helium atmosphere using Tb and Ni of 99.9% and 99.99% purity, respectively. Several single crystals with largest dimensions of approximately $4 \times 5 \times 6$ mm^3 were extracted from the ingot after slowly cooling the melt through the peritectic point. The quality and homogeneity of the single crystal were determined using x-ray Laue diffraction. Three single crystalline samples were cut along main crystallographic directions of the orthorhombic unit cell. Neutron single crystal diffraction experiments were performed at the E4 two-axis diffractometer [28] at the BER II reactor of the HZB and at the Cold Neutron Chopper Spectrometer (CNCS) [29,30] at the Spallation Neutron Source (SNS) of the Oak Ridge National Laboratory. An incident wavelength $\lambda = 2.4$ Å selected with the pyrolytic graphite PG (002) monochromator was utilized at the E4 diffractometer along with a set of $\lambda/2$ filters reducing the contamination of higher-order wavelength components to a level below 10^{-4}. The superconducting vertical field cryomagnet VM-1 capable of generating magnetic fields up to 145 kOe was used to apply magnetic field along the *c* crystallographic axis of the single crystal sample.

Neutron powder diffraction measurements were performed at the cold neutron powder diffractometer DMC [31] at the Swiss Spallation Source SINQ (Switzerland) with neutron wavelength $\lambda = 3.8$ Å. Refinement of magnetic structure was performed using JANA2006 program [32].

Magnetoresistance measurements were made in the National High Magnetic Field Laboratory (Tallahassee, FL, USA) by using an ac bridge (Lakeshore Model 372, Lakeshore, USA) under magnetic fields up to 18 T on an excitation current of 1 mA at temperatures from 1.4 K up to 300 K. Single crystalline samples with dimensions of about $2 \times 2 \times 5$ mm^3 with the long side parallel to one of the main crystallographic directions were fixed to the holder with an epoxy resin. Magnetic measurements were performed using a Magnetic Properties Measurements System (MPMS, Quantum Design, USA) in an external magnetic field up to 7 T.

III. RESULTS AND DISCUSSION

A. Zero field magnetic state

1. Magnetic susceptibility and electrical resistivity

Temperature dependence of the reciprocal magnetic susceptibility as well as zero-field cooled (ZFC) and field cooled (FC) susceptibility curves measured in an external magnetic field of 1 kOe applied along the *c* crystallographic axis are shown in Figs. 2(a) and 2(b). Our single crystal exhibits a similar temperature dependence of the magnetic susceptibility

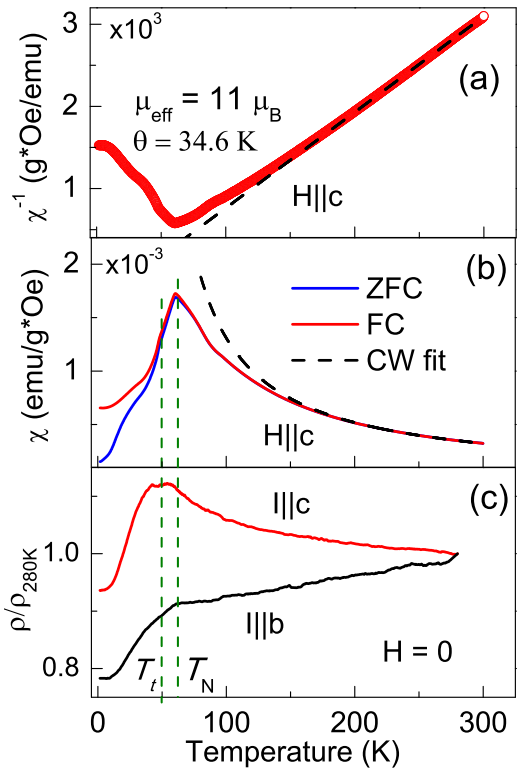

FIG. 2. (a) Reciprocal susceptibility and (b) ZFC-FC curves of magnetic susceptibility measured in applied magnetic field of 1 kOe along the c crystallographic direction. The dashed line depicts Curie-Weiss law. (c) Temperature dependence of the electrical resistivity $\rho(T)$ along the b and c crystallographic directions in zero magnetic field normalized to the electrical resistivity at $T = 280$ K.

as previously reported for the polycrystalline and single crystal samples [6,14]. ZFC-FC curves reveal significant hysteresis below the Néel temperature and a broad anomaly around $T_t \sim 50$ K. Both reciprocal and direct magnetic susceptibility curves exhibit substantial deviation from the Curie-Weiss (CW) law on cooling below 200 K. The effective magnetic moment $\mu_{\rm eff}^{\rm Tb} = 11.0\mu_B$ and paramagnetic Curie temperature $\theta_p = 34.6$ K were obtained from the CW law fit in the temperature range 220–300 K. The estimated $\mu_{\rm eff}^{\rm Tb}$ surpasses the theoretical value $\mu_{\rm eff}^{\rm Tb} = 9.72\mu_B$ for the free Tb^{3+} ion. The deviation from the CW law and an additional contribution to the effective magnetic moment arise from the enhanced short-range magnetic order persisting in Tb_3Ni over a wide temperature range up to (5–6)T_N [6]. Similar behavior was previously reported for other binary intermetallic compounds with high content of rare-earth metal such as R_3T [13,25,27], R_5Pd_2 [33], and R_7Rh_3 [34,35]. Moreover, the contribution from spin fluctuations in the d-electron subsystem may affect the susceptibility behavior as well [23,26].

Temperature dependence of the electrical resistivity measured along the b crystallographic direction [see Fig. 2(c)] exhibits a metallic behavior with a brief decrease below the Néel temperature. Such a behavior is consistent with previously reported data for the single crystal sample [25]. Contrarily, the electrical resistivity measured along the c crystallographic direction shows anomalous behavior. It is dominated by the broad hump around $T_t \sim 50$ K that is followed by monotonic decreasing when temperature is rising in a wide range above T_N. This maximum on the $\rho(T)$ curve is reminiscent of heavy rare-earth metals Ho and Dy [36], where a spiral magnetic structure results in appearance of new magnetic boundaries in the Brillouin zone and superzone gaps at the Fermi surface. Similar behavior of the electrical resistivity was reported for numerous actinide systems exhibiting emergence of complex multi-**k** magnetic structures below their Néel temperatures [37,38]. For example, an electrical resistivity maximum below the Néel temperature of the $U_{0.9}Th_{0.1}Sb$ compound was ascribed to the incommensurate to triple-**k** transition [38]. However, negative $d\rho(T)/dT$ in a wide temperature range above T_N is not typical for intermetallic systems. The negative temperature coefficient of resistivity associated with the presence of short-range antiferromagnetic correlations above T_N was detected in Gd_7Rh_3 [39]. As it has been shown in Ref. [6], short-range antiferromagnetic (AFM) correlations may persist in Tb_3Ni up to room temperature. The electron scattering on magnetic nonhomogeneities as well as the magnetic superzone gap effect inside the AFM clusters may contribute to the electrical resistivity even at temperatures well above T_N. Temperature increase suppresses the short-range AFM order and reduces the magnetic contribution to the total electrical resistivity.

2. *Single crystal neutron diffraction in zero field*

Let us turn to the low-temperature magnetic state studied in zero magnetic field. Scans across k of the $(1/2k0)$ reciprocal layer performed at several temperatures and neutron powder diffraction patterns measured at various temperatures are shown in Figs. 3(a) and 3(b), respectively. As one can see, a long-range incommensurate magnetic structure described by the incommensurate propagation vector $\mathbf{k}_{\rm IC} = [\frac{1}{2},\mu,0]$ with $\mu \approx 0.29$ develops upon cooling the sample below the Néel temperature, $T_N = 61$ K. The second commensurate propagation vector $\mathbf{k}_1 = [\frac{1}{2},\frac{1}{2},0]$ develops below 58 K. This magnetic structure persists down to $T_{f1} \sim 51$ K, where the incommensurate component partially locks in to the commensurate one with the propagation vector $\mathbf{k}_2 = [\frac{1}{2},\frac{1}{4},0]$, as it is shown in Fig. 3(c). In total, three propagation vectors $\mathbf{k}_{\rm IC}$, $\mathbf{k}_1$, and $\mathbf{k}_2$ coexist in the narrow temperature range $48 < T < 51$ K. Additional magnetic peaks indexed by $\mathbf{k}_3 = [\frac{1}{2},\frac{1}{3},0]$ and $\mathbf{k}_4 = [\frac{1}{2},0,0]$ appear around $T_{f2} \sim 48$ K while the incommensurate component completely disappears. A combination of four commensurate propagation vectors $\mathbf{k}_1$, $\mathbf{k}_2$, $\mathbf{k}_3$, and $\mathbf{k}_4$ is necessary for indexing of all the magnetic Bragg peaks in the temperature range $T < T_{f2}$. Since all of the observed propagation vectors $\mathbf{k}_i = [k_x,k_y,k_z]$ exhibit identical k_x and k_z but different k_y components, we may plot temperature dependencies of all the propagation vectors $\mathbf{k}_i$ as a phase diagram k_y versus temperature T (see Fig. 4).

The previous neutron diffraction study of the Tb_3Ni powder sample performed by Gignoux *et al.* [14] revealed two commensurate propagation vectors $\mathbf{k}_3 = [\frac{1}{2},\frac{1}{3},0]$ and $\mathbf{k}_4 = [\frac{1}{2},0,0]$ for the low-temperature magnetic state at $T = 4.2$ K while $\mathbf{k}_1$ and $\mathbf{k}_2$ were not detected, apparently due to poor resolution in the low-Q range. The multicomponent magnetic structures exhibiting coexistence of commensurate and incommensurate

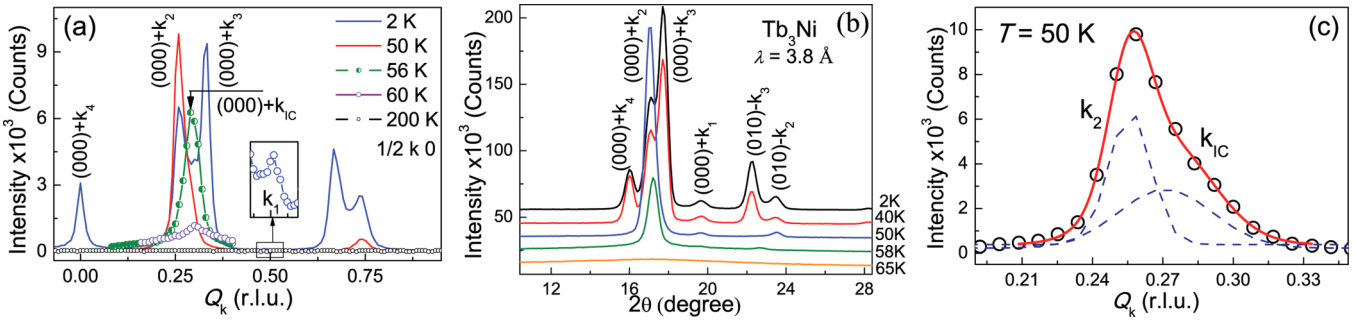

FIG. 3. (a) Scans across k of the $(1/2k0)$ reciprocal layer performed at $T = 2$, 50, 56, 60, and 200 K, (b) neutron powder diffraction patterns measured at $T = 2$, 40, 50, 58, and 65 K, and (c) scan across k of the $(1/2\,k\,0)$ reciprocal layer at $T = 50$ K. Function $I(Q_k)$ is approximated with two Gaussian components originated from $\mathbf{k}_2$ and $\mathbf{k}_{IC}$.

propagation vectors and high-order harmonics have been previously reported for other R_3Co compounds with the non-Kramers-type ions, R = Tb, Ho [12,13]. However, to our best knowledge, such a complex low-temperature magnetic state described with four different propagation vector stars $\mathbf{k}_1$, $\mathbf{k}_2$, $\mathbf{k}_3$, and $\mathbf{k}_4$ has never been observed for other R_3T compounds.

It is not possible from principal reasons to conclude from neutron diffraction data if the observed magnetic peaks belong to the several magnetic phases (magnetic phases separation scenario) or to several modulations coexisting in the one domain single crystal sample (multi-**k** structure). It should be emphasized that the observed propagation vectors $\mathbf{k}_1$, $\mathbf{k}_2$, $\mathbf{k}_3$, and $\mathbf{k}_4$ apparently are not the arms of the single **k**-star since they are not related by the symmetry elements of the space group $Pnma$. Thus the low-temperature magnetic structure of Tb_3Ni is not consistent with the multi-**k** scenario observed in numerous magnetic systems [38,40]. However, some of the observed propagation vectors still may be coupled and describe complicated magnetic structure with enlarged magnetic unit cell. The ISODISTORT program based on the ISOTROPY software package can be an effective tool for exploration of possible

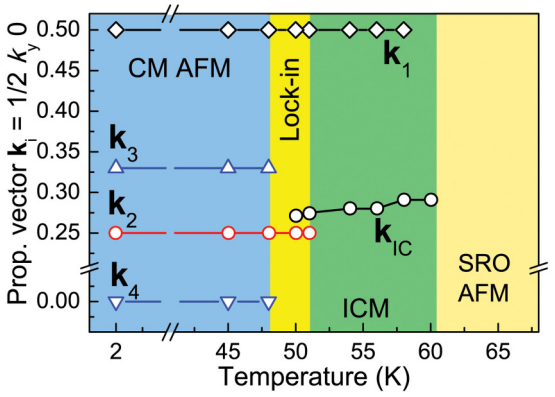

FIG. 4. Temperature dependence of the k_y components of the propagation vectors $\mathbf{k}_1$, $\mathbf{k}_2$, $\mathbf{k}_3$, $\mathbf{k}_4$, and $\mathbf{k}_{IC}$. CM AFM, antiferromagnetic phase described with the commensurate propagation vectors $\mathbf{k}_1$, $\mathbf{k}_2$, $\mathbf{k}_3$, and $\mathbf{k}_4$; Lock-in, mixed magnetic phase where incommensurate and locked-in components coexist; ICM, magnetic phase with the incommensurate magnetic structure described by $\mathbf{k}_{IC}$ and $\mathbf{k}_1$; and SRO AFM, paramagnetic state incorporating short-range antiferromagnetic clusters.

couplings between different order parameters in the system and listing of all order-parametric distortions for a group-subgroup pair [41,42].

In accordance with Ref. [41], an order parameter (OP) which defines the phase transition and determines the symmetry of the lower symmetry phase is called the primary OP. A particular direction of the OP in representation space, which is called the order parameter direction (OPD), determines a particular isotropy subgroup, the symmetry elements of which leave the OP invariant. In the case when one primary order parameter associated with one irreducible representation (irrep) is not enough to describe the symmetry of the crystal below the transition, coupling of two or more primary OPs should be considered. Experimentally observed propagation vectors $\mathbf{k}_2 = [\frac{1}{2},\frac{1}{4},0]$ and $\mathbf{k}_3 = [\frac{1}{2},\frac{1}{3},0]$ correspond to the D line of the Brillouin zone in accordance with international notation after Cracknell, Davies, Miller, and Love (CDML) [43]. In the space group $Pnma$ one four-dimensional physically irreducible representation labeled as $mD1$ can be assigned to both $\mathbf{k}_2$ and $\mathbf{k}_3$. Each irrep has general OPD with four degrees of freedom that is labeled as (a,b,c,d). A complete list of isotropy subgroups $G_{\mathbf{k}2}$ and $G_{\mathbf{k}3}$ ascribed to all possible particular directions of the OP in representation space can be generated by ISODISTORT. Coupling of two primary OPs means that symmetry of the magnetic structure below the transition is determined by the intersection of two isotropy subgroups $G_{\mathbf{k}2}$ and $G_{\mathbf{k}3}$ [44]. In total, five possible intersections $G_{\mathbf{k}2,\mathbf{k}3}$ corresponding to five particular OPDs in representation space have been found by ISODISTORT (see Table II). The OP direction classified as C2(1)C3(1) corresponds to a low-symmetry triclinic group $P_S - 1$. OPDs classified as C1(1)C2(1), C3(1)C5(1), and C3(1)C6(1) correspond to more restrictive monoclinic groups P_a2_1, P_am, and P_cc, respectively. The general OP direction of 4D1(1)4D1(1) type corresponds to the lowest symmetry triclinic group P_S1. All five models yield a magnetic supercell that is 24 times the crystallographic unit cell.

A complete list of irreps, which are capable of magnetic moments on Tb sites and can be involved in the group-subgroup transition, is shown in Table II. A combination of irreps associated with primary OPs $[\mathbf{k}_2]mD1$ and $[\mathbf{k}_3]mD1$ is mathematically capable of producing one of the five isotropy subgroups describing the low-temperature magnetic structure of Tb_3Ni. Moreover, irreps of the experimentally observed propagation vectors $\mathbf{k}_1 = [\frac{1}{2},\frac{1}{2},0]$ and $\mathbf{k}_4 = [\frac{1}{2},0,0]$ were found to be potentially involved in the phase transition as secondary OPs

TABLE II. Magnetic space groups obtained from the intersection of two isotropy subgroups associated with the irreps of two primary OPs $\mathbf{k}_2 = [\frac{1}{2},\frac{1}{4},0]$ and $\mathbf{k}_3 = [\frac{1}{2},\frac{1}{3},0]$. OP directions, basis vectors, and potentially active irreps associated with the involved secondary OPs $\mathbf{k}_1 = [\frac{1}{2},\frac{1}{2},0]$ and $\mathbf{k}_4 = [\frac{1}{2},0,0]$ are given for every magnetic space group. Particular OPDs in representation space are given in Stokes and Hatch notation [45]. Irreps symbols are given in CDML notation [43].

OPD and Shubnikov group	Basis vectors	Primary OPs	Secondary OPs
C1(1)C2(1) P_a2_1	{(−2,0,0),(0,0,1),(0,12,0)}	$[\mathbf{k}_2]mD1(a,b,b,a)$	$[\mathbf{k}_4]mX1(a,-a)$, $[\mathbf{k}_4]mX2(a,-a)$
	Origin at (−3/4,0,0)	$[\mathbf{k}_3]mD1(a,b,b,a)$	$[\mathbf{k}_1]mS1S2(0,a,0,b)$
C2(1)C3(1) P_S-1	{(0,0,1),(0,12,0),(−2,0,0)}	$[\mathbf{k}_2]mD1(a,b,0,0)$	$[\mathbf{k}_4]mX1(0,a)$, $[\mathbf{k}_4]mX2(a,0)$
	Origin at (0,0,0)	$[\mathbf{k}_3]mD1(a,b,0,0)$	$[\mathbf{k}_1]mS1S2(a,b,b,-a)$
C3(1)C5(1) P_am	{(2,0,0),(0,12,0),(0,0,1)}	$[\mathbf{k}_2]mD1(a,b,-0.414a,2.414b)$	$[\mathbf{k}_4]mX1(a,b)$
	Origin at (0,1/4,0)	$[\mathbf{k}_3]mD1(a,b,-0.577a,1.732b)$	$[\mathbf{k}_1]mS1S2(a,a,b,b)$
C3(1)C6(1) P_cc	{(0,0,1),(0,12,0),(−2,0,0)}	$[\mathbf{k}_2]mD1(a,b,-0.414a,2.414b)$	$[\mathbf{k}_4]mX2(a,b)$
	Origin at (0,13/4,0)	$[\mathbf{k}_3]mD1(a,b,1.732a,-0.577b)$	$[\mathbf{k}_1]mS1S2(a,-a,b,-b)$
4D1(1)4D1(1) P_S1	{(0,0,1),(0,12,0),(−2,0,0)}	$[\mathbf{k}_2]mD1(a,b,c,d)$	$[\mathbf{k}_4]mX1(a,b)$, $[\mathbf{k}_4]mX2(a,b)$
	Origin at (0,0,0)	$[\mathbf{k}_3]mD1(a,b,c,d)$	$[\mathbf{k}_1]mS1S2(a,b,c,d)$

coupled to the primary ones. Thus observation of magnetic satellites indexed by $\mathbf{k}_1$, $\mathbf{k}_2$, $\mathbf{k}_3$, and $\mathbf{k}_4$ at $T = 2$ K may be considered as a sign of complicated magnetic structure with a large magnetic unit cell $2a \times 12b \times c$ that is described by two coupled primary OPs and two secondary OPs rather than the magnetic phase separation scenario.

3. Neutron powder diffraction at T = 58 K

The neutron powder diffraction data were measured just below and above Néel temperature at $T = 58$ and 65 K, respectively, using a cold neutron powder diffractometer DMC (PSI, Switzerland) with the neutron wavelength $\lambda = 3.8$ Å that provides good resolution in the low-Q range. As can be seen from Fig. 5(a), a series of magnetic Bragg peaks emerges below the Néel temperature on the neutron diffraction pattern. The incommensurate magnetic structure propagation vector $\mathbf{k}_{IC} = [\frac{1}{2},\mu,0]$ determined from the single crystal neutron diffraction data has been tested by the Le Bail fit at $T =$ 58 K in order to adjust profile function parameters as well as a μ value. It has been found that the high-intensity magnetic satellite of $(000)^+$ type having a slightly asymmetric shape and a substantial magnetic critical scattering contribution could not be well approximated on the refinement. Thus, the low-angle range $2\theta < 25^\circ$ was excluded from the refinement. The Le Bail fitting of the neutron diffraction pattern within the angle range $25^\circ < 2\theta < 131^\circ$ revealed that the propagation vector $\mathbf{k}_{IC}$ with the k_x component fixed to 1/2 and an adjustable k_y component is able to index all the magnetic satellites. However, the fit quality was not perfect, indicating that the k_x component needs to be adjusted as well. The second refinement with both k_x and k_y adjustable parameters provided the best fit quality and revealed slight deviation of k_x from the commensurate value. The incommensurate magnetic structure propagation vector was estimated to be $\mathbf{k}_{IC} = [\frac{1}{2}+\delta,\mu,0]$, where $\delta = 0.006 \pm 0.001$ and $\mu = 0.299 \pm 0.001$.

In the case of the orthorhombic crystal structure with the space group $Pnma$, the propagation vector star $\mathbf{k}_{IC}$ (CDML label V of Brillouin zone) has four arms $\mathbf{k}^1_{IC} = [k_x,k_y,0]$, $\mathbf{k}^2_{IC} = [-k_x,k_y,0]$, $\mathbf{k}^3_{IC} = [k_x,-k_y,0]$, and $\mathbf{k}^4_{IC} = [-k_x,-k_y,0]$, where $k_x = 0.506$ and $k_y = 0.299$. Two symmetry operations of the space group $Pnma$ $\{E|000\}$ and $\{m_z|\frac{1}{2}0\frac{1}{2}\}$ leaving the propagation vector $\mathbf{k}_{IC}$ invariant form the little group $G_\mathbf{k}$. Magnetoactive terbium atoms occupy two nonequivalent crystallographic sites Tb1($4c$: 0.0294,0.25,0.3556) and Tb2($8d$: 0.1800,0.0649,0.8209) in the Tb_3Ni structure. These sites are split in two and four independent magnetic orbits, respectively, by the symmetry operations of the little group $G_\mathbf{k}$. Decomposition of the magnetic representation of the little group $G_\mathbf{k}$ performed with BASIREPS program [46] gives two one-dimensional irreducible representations $\Gamma_{MAG} = 3\Gamma_1 + 3\Gamma_2$ for both $4c$ and $8d$ magnetic Tb atoms. Then three basis vectors for every of six independent magnetic orbits can be constructed. In total, one should refine 18 mixing coefficients of basis vectors and 5 relative phases between independent magnetic orbits in order to test both the irreducible representations unless some restriction may be imposed.

Alternatively, one can introduce the magnetic moment modulation functions defined in the $(3+1)$-dimensional superspace and describe the magnetic structure using magnetic superspace group formalism [47–50]. The magnetic moment modulation function $\mathbf{M}_i$ describes the magnetic moment of an atom i with atomic coordinates $\mathbf{r}_i$ in the unit cell shifted by a lattice translation $\mathbf{T}$ from the zeroth unit cell and can be represented as a Fourier series [49]:

$$\mathbf{M}_i(x_4) = \mathbf{M}_{i,0} + \sum_{n=1}^{N}\left[\mathbf{M}^{\sin}_{i,n}\sin(2\pi n x_4) + \mathbf{M}^{\cos}_{i,n}\cos(2\pi n x_4)\right], \tag{1}$$

where n is a number of terms in Fourier series that is limited to $n = 1$, $x_4 = \mathbf{k}(\mathbf{T}+\mathbf{r}_i)$ is an internal coordinate, and absolute term $\mathbf{M}_{i,0} = 0$ since there is no ferromagnetic component at $T = 58$ K. Magnetic moment modulation functions $\mathbf{M}_i(x_4)$ and $\mathbf{M}_j(x_4)$ of the symmetry-related atoms $\{\mathbf{R}|\mathbf{t}\}\mathbf{r}_i = \mathbf{r}_j + \mathbf{T}$ in the unit cell are constrained by the symmetry operations of the magnetic superspace group in a four-dimensional space $\{\mathbf{R},\theta|\mathbf{t},\tau\}$ in a way determined by the following equation for the purely incommensurate propagation vector $\mathbf{k}_{IC}$ [49]:

$$\mathbf{M}_j(R_I x_4 + \tau_0) = \theta\det(\mathbf{R})\mathbf{R}\mathbf{M}_i(x_4), \tag{2}$$

where $\tau_0 = \tau + \mathbf{kt}$, R_I equals $+1$ for $\mathbf{R}$ keeping $\mathbf{k}$ invariant or -1 for the one transforming $\mathbf{k}$ to $-\mathbf{k}$, and θ is a time-reversal

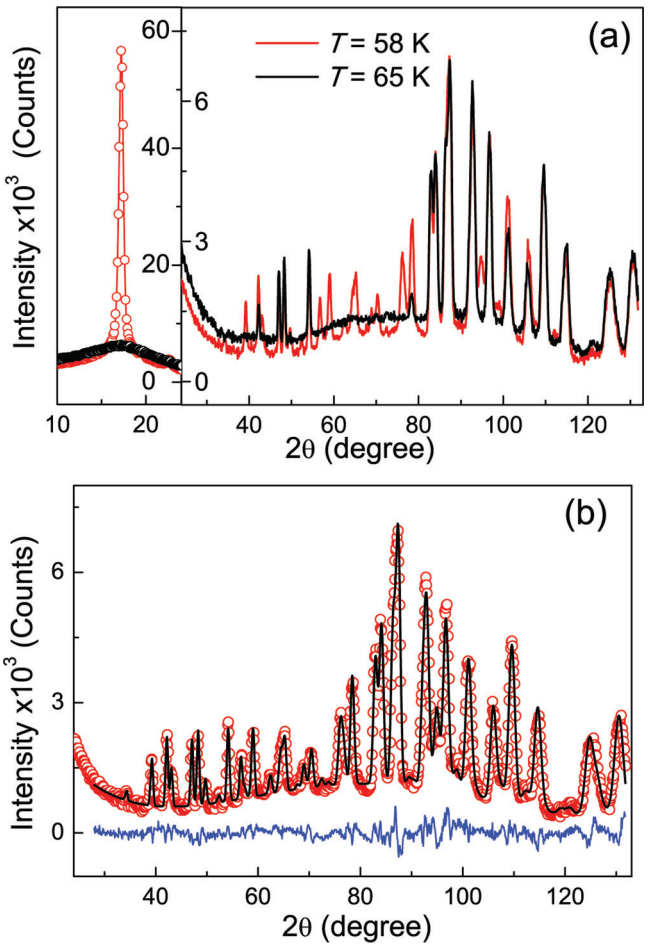

FIG. 5. (a) Neutron powder diffraction patterns for Tb_3Ni measured at $T = 58$ and 65 K. (b) The results of Rietveld refinement of the neutron diffraction pattern at $T = 58$ K using the model of the magnetic superspace group $P112_1/a1'(ab0)0ss$. Open circles represent the experimental profile, the black line through the symbols is the model profile, and the solid line at the bottom is the difference curve.

operation that could be $+1$ or -1 for a particular symmetry operator of the magnetic superspace group.

In order to determine the superspace group of the magnetic structure, symmetry of the parent paramagnetic phase described with the magnetic grey space group $Pnma1'$ should be considered. This space group consists of all symmetry operations of the space group $Pnma$ and the equal number of operations multiplied by the time-reversal operator $1'$. The little co-group $G_{\mathbf{k}}$ of the propagation vector $\mathbf{k}$ consists of all symmetry operations keeping the propagation vector $\mathbf{k}$ invariant. All the symmetry operations of the little co-group $G_{\mathbf{k}}$ and those ones transforming propagation vector $\mathbf{k}$ to $-\mathbf{k}$ form a subgroup of the paramagnetic space group that is called an extended little group. The little co-group for $\mathbf{k}_{IC} = [0.506,0.299,0]$ is composed of four symmetry operations $\{E,m_z,1',m_z'\}$ and can be defined as a grey magnetic point group $m1'$. There are two magnetic irreps of the paramagnetic space group $Pnma1'$ which are trivially related (see Ref. [49]) to the irreducible representations of the little co-group $m1'$ shown in Table III. In accordance with Landau theory of second-order phase transitions, the magnetic structure of Tb_3Ni below its Néel temperature involves one of these magnetic irreps to which a particular magnetic superspace group can be assigned.

TABLE III. Irreducible representations of the little co-group $m1'$ for $\mathbf{k}_{IC} = [0.506,0.299,0]$ which define two possible magnetic irreps of the paramagnetic space group $Pnma1'$. Two corresponding magnetic superspace groups are shown in the last column ($a = \exp\{2\pi \times 0.253\}$).

Irreps	E	m_z	$1'$	Superspace group
mV_1	1	a	-1	$P112_1/a1'(ab0)00s$
mV_2	1	$-a$	-1	$P112_1/a1'(ab0)0ss$

As it has been shown in Ref. [49], a magnetic superspace group includes all the symmetry operations of the extended little group together with the time-reversal operator $\{1'|000\frac{1}{2}\}$. Additionally a translation of $\{000\frac{1}{2}\}$ should be added to the symmetry operations of the little co-group having character -1. Thus, two magnetic superspace groups $P112_1/a1'(ab0)00s$ and $P112_1/a1'(ab0)0ss$ can be constructed manually or automatically generated by the JANA2006 program [32]. Symmetry operations for both magnetic superspace groups are presented in Table IV in accordance with formalism used in JANA2006. Both of these groups could be transformed to the standard setting $P2_1/c1'(a0g)00s$ and $P2_1/c1'(a0g)0ss$ applying the following transformation:

$$\begin{pmatrix} a' \\ b' \\ c' \end{pmatrix} = \begin{pmatrix} 0 & 1 & 0 \\ 0 & 0 & 1 \\ 1 & 0 & 0 \end{pmatrix} \times \begin{pmatrix} a \\ b \\ c \end{pmatrix}. \quad (3)$$

It should be emphasized that involvement of the symmetry operations transforming $\mathbf{k}$ to $-\mathbf{k}$ allows one to avoid splitting of the $4c$ and $8d$ Wyckoff sites of the Tb_3Ni crystal structure to six completely independent magnetic orbits obtained within the representation analysis approach. In the magnetic superspace group approach, one has three symmetrically nonequivalent magnetic sites Tb1 ($4c$: 0.0309, 0.25, 0.3562), Tb2 ($8d$: 0.1800, 0.0651, 0.8209), and Tb3 ($8d$: 0.8200, 0.5651, 0.1791) which are general fourfold positions for $P112_1/a$ space group. The magnetic superspace group gives no constraints on the possible orientation of the magnetic moments of three symmetrically nonequivalent magnetic Tb sites. However, relations between components of the magnetic moment modulation functions $\mathbf{M}_i(x_4)$ of the Tb atoms occupying the general fourfold site are determined by the symmetry operations of the magnetic superspace group in accordance with Eq. (2). These relations are shown in Table V for magnetic superspace group $P112_1/a1'(ab0)0ss$. Thus, three $\mathbf{M}_i^{\sin}$ components and three $\mathbf{M}_i^{\cos}$ components for every magnetic Tb site should be refined.

The Rietveld refinement performed using the JANA2006 program revealed that the $P112_1/a1'(ab0)0ss$ magnetic superspace group provides significantly better agreement factors as well as good quality of fit. The refined magnetic parameters are shown in Table VI. The refined magnetic structure represents a combination of three spin-density-wave (SDW)-like modulations over Tb1, Tb2, and Tb3 magnetic orbits propagating along the b crystallographic direction. The SDW over the Tb1

TABLE IV. Representative operations of the magnetic superspace groups $P112_1/a1'(ab0)00s$ and $P112_1/a1'(ab0)0ss$ and their symmetry cards generated by the program JANA2006 [32]. The symbols $-m$ and m label symmetry operations with and without time reversal, respectively. A complete set of symmetry operations can be obtained from the presented ones by the internal product of the group.

	$P112_1/a1'(ab0)00s$	$P112_1/a1'(ab0)0ss$
$\{E\|0000\}$	x_1,x_2,x_3,x_4,m	x_1,x_2,x_3,x_4,m
$\{2_z\|\frac{1}{2}0\frac{1}{2}0\}$	$-x_1+\frac{1}{2},-x_2,x_3+\frac{1}{2},-x_4,m$	$-x_1+\frac{1}{2},-x_2,x_3+\frac{1}{2},-x_4+\frac{1}{2},m$
$\{\bar{1}\|0000\}$	$-x_1,-x_2,-x_3,-x_4,m$	$-x_1,-x_2,-x_3,-x_4,m$
$\{m_z\|\frac{1}{2}0\frac{1}{2}0\}$	$x_1+\frac{1}{2},x_2,-x_3+\frac{1}{2},x_4,m$	$x_1+\frac{1}{2},x_2,-x_3+\frac{1}{2},x_4+\frac{1}{2},m$
$\{1'\|000\frac{1}{2}\}$	$x_1,x_2,x_3,x_4+\frac{1}{2},-m$	$x_1,x_2,x_3,x_4+\frac{1}{2},-m$

site is almost confined within the propagation plane that is parallel to the b crystallographic direction and inclined from the c axis to the a crystallographic axis by an angle of $\theta_{ac}^{\mathrm{Tb1}}$. The SDWs over Tb2 and Tb3 magnetic orbits are almost confined within the propagation planes that are inclined by similar angles $\theta_{ac}^{\mathrm{Tb2}}$ and $\theta_{ac}^{\mathrm{Tb3}}$ in the opposite direction from the c axis. These SDW modulations exhibit the slight out-of-plane fluctuations comparable with the standard deviations that may arise from the fit imperfections. The difference between waves over Tb1, Tb2, and Tb3 sites can be seen in the projection on the bc crystallographic plane. The SDW over the Tb1 site seems to be almost transverse having a y component comparable with the standard deviation. Contrarily, magnetic moments of the SDW over Tb2 and Tb3 sites slightly fluctuate around directions that are inclined from the c axis to the b axis in opposite directions by similar angles of $-\phi_{bc}^{\mathrm{Tb2}}$ and ϕ_{bc}^{Tb3}.

Thus, additional restrictions that are not defined by the magnetic superspace group symmetry can be imposed: (i) $\theta_{ac}^{\mathrm{Tb1}}=-\theta_{ac}^{\mathrm{Tb2}}=-\theta_{ac}^{\mathrm{Tb3}}$, (ii) $\phi_{bc}^{\mathrm{Tb3}}=-\phi_{bc}^{\mathrm{Tb2}}$, and (iii) out-of-plane components for all SDW modulations were manually fixed to zero. The constrained model of the magnetic structure has been refined and its magnetic parameters are shown in Table VI. The best fit result is shown in Fig. 5(b). The schematic visualization of the constrained magnetic structure is shown in Fig. 6. It should be emphasized that a slight deviation of the k_x component of the propagation vector $\mathbf{k}_{\mathrm{IC}}=[0.506,0.299,0]$ from the commensurate value $k_x=0.5$ means a very long period spin-wave modulation ($l\sim 1140$ Å) along the a crystallographic axis (not shown in Fig. 6).

B. Field-induced magnetic state

1. Field applied along the a crystallographic axis

The magnetoresistance curves $\Delta\rho(H)/\rho(0)$ measured at various temperatures as a function of an external magnetic field applied along the a crystallographic axis are shown in Figs. 7(a)–7(c). At low temperature of 1.5 K, the $\Delta\rho(H)/\rho(0)$ curve exhibits a two-steps-like drop down to -49% at the critical fields $H_{\mathrm{C1}}^{up}=120$ kOe and $H_{\mathrm{C2}}^{up}=142$ kOe. This is in agreement with the field dependence of the magnetization reported in Ref. [14] and can be ascribed to suppression of the magnetic superzone gaps at the Fermi surface due to two successive magnetic phase transitions from the AFM state via an intermediate ferrimagnetic (IFIM)-type state to the forced ferromagnetic (FM) state. A similar magnetoresistance upon application of external magnetic field was previously reported for numerous binary rare-earth intermetallic compounds [10,11,27,39,51]. A substantial hysteresis of $\Delta\rho(H)/\rho(0)$ vs H curves measured on magnetization and demagnetization persists in a wide magnetic field range below H_{C2}^{up}. The magnetoresistance curve measured on demagnetization exhibits similar two-step behavior with the FM-IFIM phase transition at the critical field H_{C2}^{dwn} and IFIM-AFM phase transition at H_{C1}^{dwn}. Temperature increasing up to 40 K results in suppression of the hysteresis behavior and in reduction of H_{C1} and H_{C2}. It should be emphasized that the magnetoresistance curves with an inflection point are observed to persist up to 80 K, which is well above $T_{\mathrm{N}}=61$ K. Such an unusual behavior may originate from suppression of the short-range AFM order persisting in Tb_3Ni up to temperatures that are five to six times greater than the Néel temperature [6]. The magnetic phase diagram for a Tb_3Ni single crystal in an external magnetic field applied along the a crystallographic direction is shown in Fig. 8(a).

TABLE V. Relations between components of the magnetic moment modulation functions $\mathbf{M}_i(x_4)$ of the general fourfold site produced by the symmetry operations of the magnetic superspace group $P112_1/a1'(ab0)0ss$.

	Components of $\mathbf{M}_i(x_4)$		
$\{E\|0000\}$	$M_x(x_4)$	$M_y(x_4)$	$M_z(x_4)$
$\{2_z\|\frac{1}{2}0\frac{1}{2}0\}$	$-M_x(x_4+\frac{1}{2})$	$-M_y(x_4+\frac{1}{2})$	$M_z(x_4+\frac{1}{2})$
$\{\bar{1}\|0000\}$	$M_x(-x_4)$	$M_y(-x_4)$	$M_z(-x_4)$
$\{m_z\|\frac{1}{2}0\frac{1}{2}0\}$	$-M_x(x_4+\frac{1}{2})$	$-M_y(x_4+\frac{1}{2})$	$M_z(x_4+\frac{1}{2})$

2. Field applied along the b crystallographic axis

The magnetoresistance curves $\Delta\rho(H)/\rho(0)$ measured at various temperatures as a function of the external magnetic field applied along the b crystallographic axis are represented in Figs. 7(d)–7(f). As one can see, magnetoresistance behavior at low temperatures is substantially different from the data obtained for the field applied along the a direction. The magnetoresistance curve measured at $T=4$ K exhibits step-like decrease of -44% at the critical magnetic field $H_{\mathrm{C}}^{up}=118$ kOe that corresponds to the metamagnetic transition to the forced FM state, as it was reported by Gignoux *et al.* [14] from the field dependence of the magnetization measured on the single-crystal sample. Some hysteresis upon demagnetization can be observed on the magnetoresistance data in our work as well as on the magnetization data in work [14].

However, the magnetoresistance curve measured on demagnetization changes dramatically below 4 K. At $T=1.5$ K

TABLE VI. Refined components of the high-temperature incommensurate magnetic moment modulation functions $\mathbf{M}_i^{\sin}$ and $\mathbf{M}_i^{\cos}$ obtained for the symmetrically nonequivalent magnetic sites Tb1, Tb2, and Tb3 using symmetry relations of the magnetic superspace group $P112_1/a1'(ab0)0ss$ without any additional restrictions (upper table) and with additional restrictions as it is described in the text (bottom table). The maximum value of the terbium magnetic moment is given in the last column.

	$M_x^{\sin}(\mu_B)$	$M_y^{\sin}(\mu_B)$	$M_z^{\sin}(\mu_B)$	$M_x^{\cos}(\mu_B)$	$M_y^{\cos}(\mu_B)$	$M_z^{\cos}(\mu_B)$	$\lvert M\rvert_{\max}(\mu_B)$
Tb1	0.424(213)	−0.048(237)	1.854(124)	1.422(227)	−0.269(194)	4.420(124)	5.0(0.3)
Tb2	−1.252(186)	−2.535(145)	4.958(120)	−0.425(273)	−1.134(280)	0.885(106)	5.9(0.3)
Tb3	1.035(172)	−0.834(174)	−2.254(101)	−1.106(250)	0.700(235)	2.516(128)	3.9(0.3)
$R_F^{nucl}(obs) = 1.9\%$, $R_F^{mag}(obs) = 2.9\%$, $R_P = 2.8\%$, $wR_P = 3.4\%$							
Tb1	0.545(29)	0[a]	1.702(85)	1.426(31)	0[a]	4.457(89)	5.0(0.1)
Tb2	−1.579(26)	−2.100(49)	4.935(76)	−0.307(26)	−0.408(49)	0.959(76)	5.7(0.1)
Tb3	0.731(28)	−0.972(53)	−2.285(82)	−0.875(27)	1.164(51)	2.735(79)	4.0(0.1)
$R_F^{nucl}(obs) = 2.0\%$, $R_F^{mag}(obs) = 3.2\%$, $R_P = 2.9\%$, $wR_P = 3.4\%$							

[a] Manually fixed.

the magnetoresistance curve on demagnetization exhibits an increase at the critical field $H_{C1}^{dwn} \sim 101$ kOe that is followed by decreasing below $H_{C2}^{dwn} \sim 81$ kOe down to the value previously observed for the forced FM state. The further field cycling keeps the sample in the metastable FM state within the field ranges $-H_{C2}^{dwn} < H < H_{C2}^{dwn}$, $H > H_{C1}^{dwn}$, and $H < -H_{C1}^{dwn}$ and in the metastable magnetic state that is formed by mixture of the ferromagnetic and antiferromagnetic phases (FM + AFM) in the field ranges $H_{C2}^{dwn} < H < H_{C1}^{dwn}$ and $-H_{C1}^{dwn} < H < -H_{C2}^{dwn}$. As seen in Fig. 7(e), a temperature increase up to 3 K almost suppresses the metastable magnetic states observed at $T = 1.5$ K. The further temperature rise up to 60 K, that is just below $T_N = 61$ K, results in suppression of the hysteresis behavior and gradual transition to the forced FM state. Similar monotonic decrease of the magnetoresistance curve due to the suppression of the short-range antiferromagnetic order can be observed at the temperatures well above T_N [see Fig. 7(f)]. The magnetic phase diagram for the Tb_3Ni single crystal in an external magnetic field applied along the b crystallographic axis is shown at Fig. 8(b).

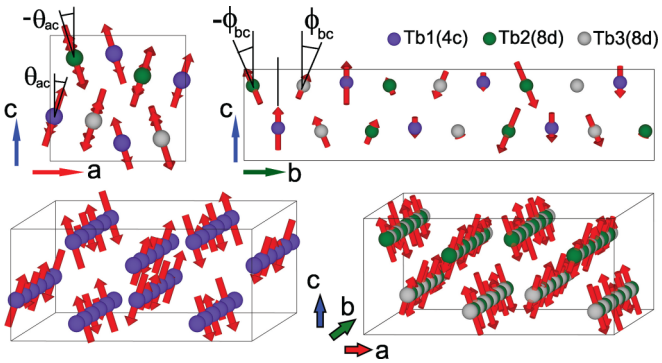

FIG. 6. Schematic visualization of the SDW magnetic structure for the high-temperature incommensurate magnetic phase of Tb_3Ni. Projections of the $a \times 3b \times c$ crystallographic cell on the ac crystallographic plane is shown on the top left. Projections of the $\frac{1}{2}a \times 3b \times c$ crystallographic cell on the bc crystallographic plane is shown on the top right. 3D visualization of the SDW magnetic modulations over Tb1($4c$) site and the ones over Tb2($8d$) and Tb3($8d$) magnetic sites for the $2a \times 6b \times c$ crystallographic cell are shown at the bottom left and right, respectively.

3. *Field applied along the c crystallographic axis*

In Figs. 9(a)–9(f), we plot magnetization and magnetoresistance curves measured below and above T_N in an external magnetic field applied along the c crystallographic direction that is the easy magnetization axis for Tb_3Ni [14]. At $T = 2$ K, application of an external magnetic field above $H_C = 54$ kOe results in a step-like jump of the magnetization reaching the saturation. Since the critical magnetic field H_C of the magnetoresistance jump coincides with H_C of the magnetization jump at $T = 1.5$ K, the critical field of the AFM-FM phase transition can be determined from both magnetization and magnetoresistance curves. The magnetic moment per Tb ion does not reach its theoretical value $gJ = 9\mu_B$ even in the magnetic field of 75 kOe. This inconsistence results from the presence of a large magnetocrystalline anisotropy due to the crystal field effect and noncollinearity of the magnetic structure even in the field-induced FM state [14]. The hysteresis keeps the sample in the metastable ferromagnetic (MFM) state in zero field and one needs to apply negative magnetic field of $H_{C1}^{dwn} = -13$ kOe to reinstate the AFM state. The second step-like metamagnetic transition from the AFM state to the forced FM state can be observed at the critical field $H_{C2}^{dwn} = -53.5$ kOe. Thus, one can observe a wide symmetric hysteresis loop of the "wasp-waisted" type with two sharp magnetization jumps at the critical fields H_{C1}^{dwn}, H_{C2}^{dwn} on field decreasing and two jumps at H_{C1}^{up}, H_{C2}^{up} on field increasing, as it is shown in Fig. 9(a). The sharpness of the step-like transitions showed by both magnetization and magnetoresistance curves may be ascribed to the simultaneous domain wall motion on the scale of the sample, due to a thermal "avalanche effect," initiated by wall tunneling events on a microscopic scale. Temperature increase up to 4 K results in a substantial change of the hysteresis loop: (i) the critical field values decrease, (ii) the wasp-waisted shape of the hysteresis loop is almost lost, (iii) the field-induced metamagnetic transitions on the hysteresis loop evolve to be smooth, and (iv) decreasing of the field to zero still keeps the sample in the metastable FM state while application of a negative magnetic field below $H_{C1}^{dwn} \sim -9.5$ kOe partially suppresses ferromagnetism and induces the mixed AFM + FM magnetic state.

The further increase of temperature up to 10 K restores the wasp-waisted shape of the hysteresis loop and suppresses zero-field metastable ferromagnetic state. The critical fields H_C,

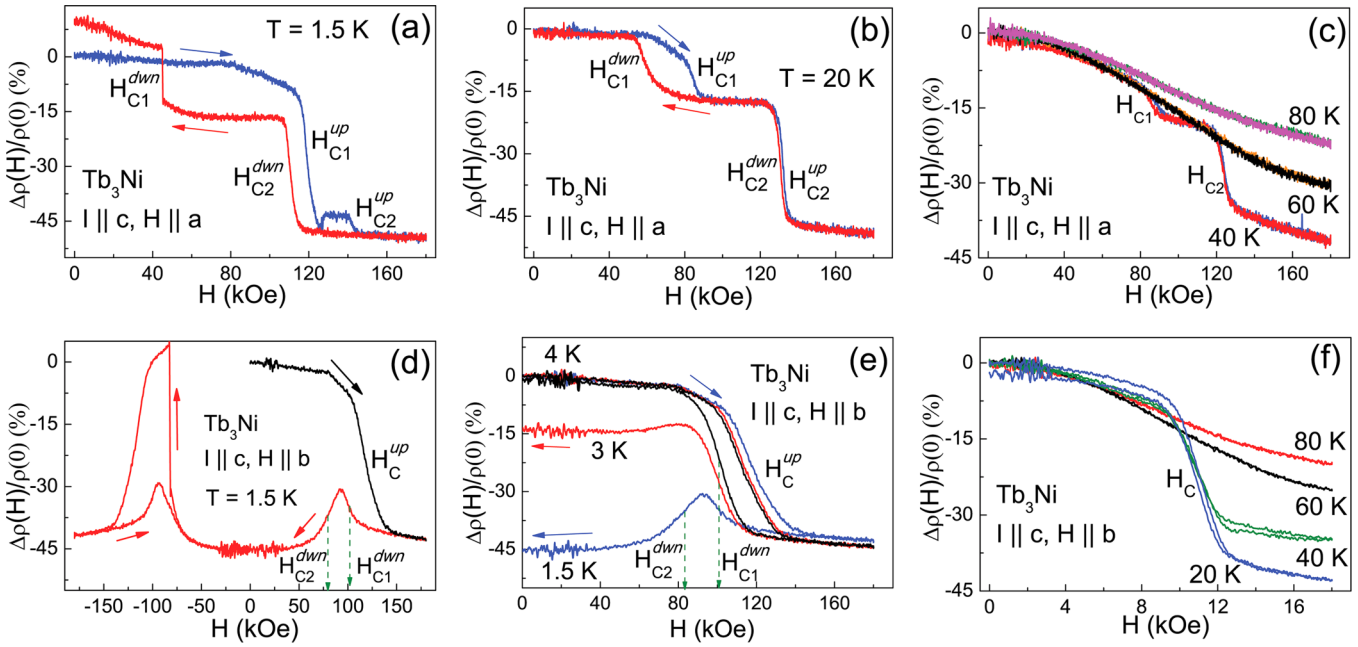

FIG. 7. Magnetoresistance curves measured in a geometry with the current along the c crystallographic direction and magnetic field (a)–(c) along the a axis and (d)–(f) along the b axis at different temperatures.

H_{C2}^{dwn} and the hysteresis loop width $\Delta H = H_{C2}^{up} - H_{C2}^{dwn} = H_{C1}^{up} - H_{C1}^{dwn}$ monotonically decrease, as shown in Figs. 10(a) and 10(b). The magnetic hysteresis is almost suppressed on heating up to 40 K while the critical field $H_C = H_{C1} = -H_{C2}$ reaches its lowest value. Surprisingly, the critical field value H_C corresponding to the magnetization and magnetoresistance jumps at $T = 60$ K and inflection points on the both curves at 80 K increase on heating above $T_N = 61$ K. As it has been shown in Ref. [6], the non-Brillouin shape of the field dependence of the magnetization well above the Néel temperature can be explained by an enhanced short-range AFM order persisting up to temperatures that are five to six times greater than T_N. Thus, the enhanced critical field at 80 K may be attributed to the field-induced AFM-FM phase transition within the AFM clusters.

The temperature dependence of the hysteresis loop width ΔH shown on Fig. 10(b) exhibits exponential rather than the power law behavior. The power law following an empirical formula $H_C(T)/H_C(0) = -V_t T + [1 + (V_t T)^2]^{1/2}$, where V_t represents the degree of easiness for thermally activated movement of domain walls, was used for modeling of a thermally activated domain walls displacement in ferromagnets with a high uniaxial anisotropy [52–54]. The exponential decay of the coercive field following an empirical formula $H_C(T)/H_C(0) = \exp(-\alpha T)$ is typically observed in a numerous amorphous systems where random magnetic anisotropy plays a crucial role [55]. The effect of averaging in amorphous materials results in a faster decrease in the anisotropy constant K_{ave} with temperature and thus in a faster decrease in H_C than in crystalline materials [56]. This mechanism seems to be irrelevant

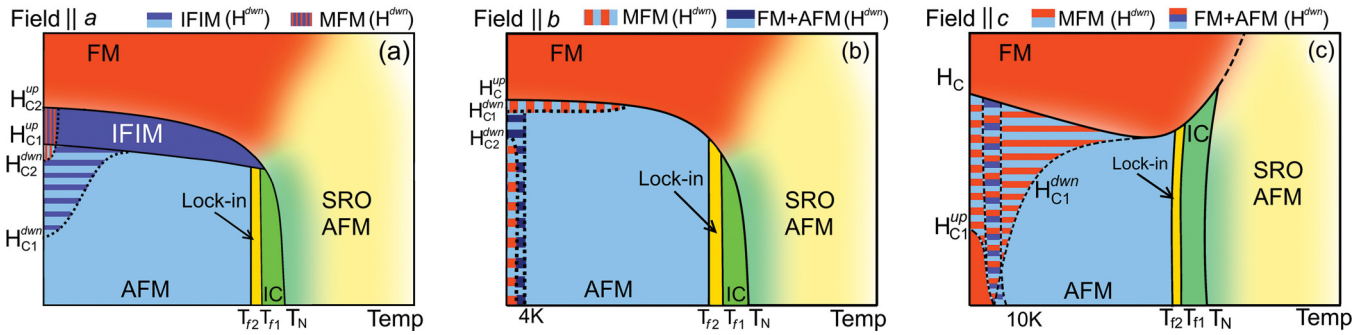

FIG. 8. Magnetic phase diagrams plotted using temperature dependencies of the critical fields obtained from the magnetoresistance and magnetic measurements in a geometry with magnetic field (a) along the a axis, (b) along the b axis, and (c) along the c axis. Solid and dotted lines represent phase boundaries on the initial magnetization and demagnetization, respectively. SRO AFM denotes a paramagnetic state with short-range antiferromagnetic order; FM, forced ferromagnetic state; AFM, low-temperature antiferromagnetic state; IC, high-temperature incommensurate magnetic state just below the Néel temperature; Lock-in, mixed magnetic state with partially locked-in incommensurate component; MFM, metastable ferromagnetic state persisting on demagnetization; IFIM, an intermediate ferrimagnetic state; FM+AFM, metastable mixed magnetic state below 4 K where both ferromagnetic and antiferromagnetic phases coexist.

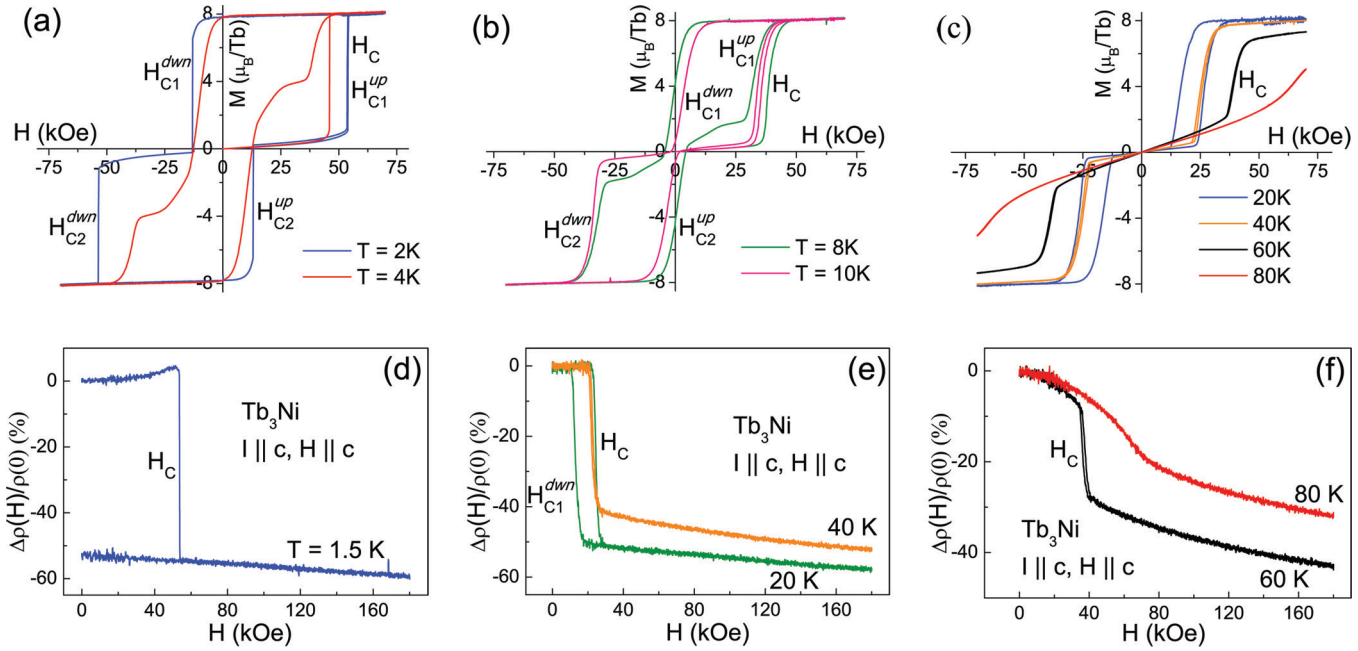

FIG. 9. (a)–(c) Hysteresis loops and (d)–(f) magnetoresistance curves measured in a geometry with magnetic field applied along the c axis and current along the c crystallographic direction in a wide range of temperatures below and above T_N.

for the structurally ordered Tb_3Ni single crystal possessing the orthorhombic symmetry. A more reliable scenario may be suggested if one takes into account that the magnitude of the crystal field in R_3T-type compounds is stronger than the exchange interactions [6,14]. A strong anisotropy implies that Tb magnetic moments are constrained to be either parallel or antiparallel to the local easy axis, as it is supposed for Ising-like magnetic systems. A rapid decay of large magnetic hysteresis on heating was reported for isostructural Tb_3Co compound exhibiting the Ising-like magnetic state at low temperatures [13]. In accordance with Ref. [57], the value of the critical magnetic field necessary for the metamagnetic transition from the AFM state to the forced FM state as well as the hysteresis value in the Ising-like systems are controlled by the local exchange interaction between neighboring Tb moments and thermal activation rather than by the anisotropy energy, as it is usually observed in high-anisotropic ferromagnetic compounds. However, to our best knowledge, there is no strict theory explaining the empirical formula of the exponential decay of the coercive field in the structurally ordered Ising-like magnetic systems.

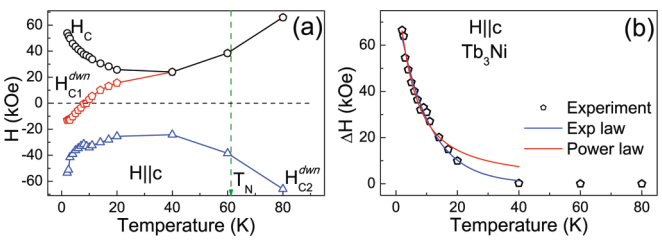

FIG. 10. (a) Temperature dependence of the critical fields H_C, H_{C1}^{dwn}, and H_{C2}^{dwn} obtained from the field dependencies of magnetization measured below and above T_N. (b) Temperature dependence of the hysteresis loop width ΔH fitted by exponential and power laws (see the text).

We performed a neutron diffraction experiment on the single-crystal sample in an external magnetic field applied along the c crystallographic axis in order to prove the existence of an intriguing zero-field metastable ferromagnetic state at low temperature $T = 2$ K in Tb_3Ni. Scans across k of the $(1/2\,k\,0)$ reciprocal layer performed at $T = 2$ K in the zero magnetic field and in external magnetic fields 40 and 120 kOe applied along the c axis are shown in Fig. 11(a). It can be seen that an external magnetic field 120 kOe completely suppresses all magnetic satellites indexed by the propagation vectors $\mathbf{k}_1$, $\mathbf{k}_2$, $\mathbf{k}_3$, and $\mathbf{k}_4$. The detailed field dependencies of the integral intensity of two nuclear Bragg peaks (120) and (220) as well as of two antiferromagnetic satellites $(1/2\ 1/4\ 0)$ and $(1/2\ 1/3\ 0)$ are shown in Figs. 11(b) and 11(c), correspondingly. It can be seen that application of external magnetic field above $H_C \sim 50$ kOe results in suppression of the magnetic satellites and enhancement of the integral intensity of the nuclear Bragg peaks due to a ferromagnetic contribution. Decreasing of the field to zero keeps the sample in the metastable ferromagnetic state, which is in agreement with our magnetization and magnetoresistance data. The magnetic phase diagram for Tb_3Ni single crystal in an external magnetic field applied along the c crystallographic direction is shown in Fig. 8(c).

IV. SUMMARY AND CONCLUSION

There are plenty of theoretical and experimental studies on geometrically frustrated nonmetallic lattices with Ising anisotropy that reveal commensurate and incommensurate multicomponent magnetic structures as well as complex magnetic phase diagrams exhibiting a rich variety of field-induced phase transitions [58,59]. As it has been shown in Ref. [6], Tb_3Ni at low temperatures is an example of a metallic Ising-like magnetic system with substantial frustration of exchange interactions of different types. Particularly, two distinct

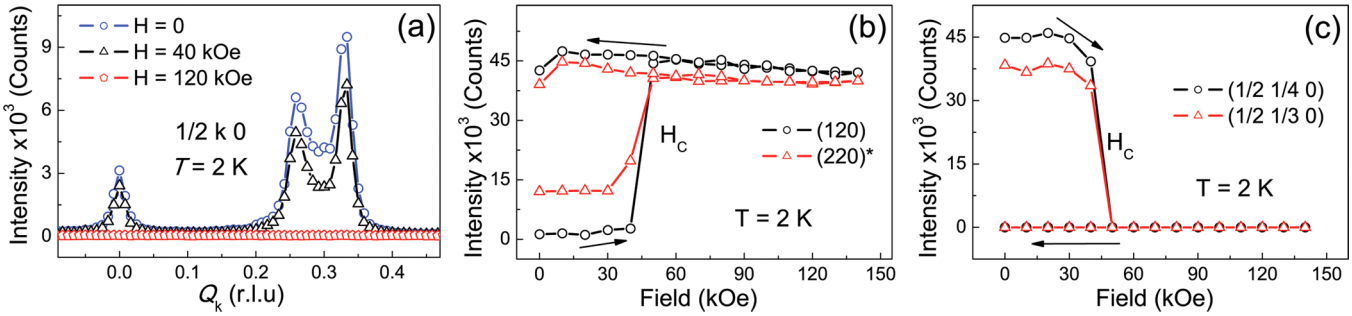

FIG. 11. (a) Scans across k of the $(1/2\,k\,0)$ reciprocal layer performed at $T = 2$ K in the external magnetic fields 0, 40, and 120 kOe applied along the c crystallographic direction. (b, c) Detailed field dependencies of the integral intensity of nuclear Bragg peaks (120) and (220) (reduced by factor 2) and antiferromagnetic satellites (1/2, 1/4, 0) and (1/2 1/3 0) measured on magnetization and demagnetization at $T = 2$ K.

indirect exchange interaction mechanisms compete in the R_3T compounds between R ions revealing as short distances as in the pure rare-earth metals. As in other rare-earth transition-metal intermetallic compounds, the indirect $4f$-$4f$ exchange coupling [60] through $4f$-$5d$-$3d$-$5d$-$4f$ mechanism and $5d$-$3d$ hybridization apparently dominates between the buckled layers of the R_3T structure. As in pure rare-earth metals, $4f$-$4f$ indirect exchange via $4f$-$5d$ intra-atomic interaction and short-range $5d$-$5d$ interaction between neighboring R ions is enhanced within the buckled layers of the R_3T structure and gives rise to the short-range magnetic order persisting in Tb_3Ni up to temperatures that are five to six times greater than T_N [6]. The complex magnetic phase diagram exhibiting a series of the field- and temperature-induced magnetic phase transitions as well as an unusual metastable ferromagnetic state stabilized at low temperatures after application of an external magnetic field, as it was evidenced by neutron diffraction, magnetization, and magnetoresistance measurements on a Tb_3Ni single crystal sample, arise from the competition of the low-symmetry crystal electric field and RKKY exchange interactions of different types. The Ising-like magnetic state with substantial frustration in the magnetic subsystem may give rise to the exponential law of the hysteresis loop width $\Delta H(T)$, observed in a geometry with a magnetic field applied along the c crystallographic axis.

The complexity of the low-temperature magnetic structures in Tb_3Ni was evidenced by our single crystal and powder neutron diffraction data. The incommensurate magnetic structure with the propagation vector $\mathbf{k}_{IC} = [0.506, 0.299, 0]$ emerges in Tb_3Ni on cooling below the Néel temperature $T_N = 61$ K. We have performed refinement of the high-temperature incommensurate magnetic structure of Tb_3Ni using the magnetic superspace groups formalism that was found to be more efficient and more restrictive than the conventional representation analysis. Additional restrictions arise from the fact that some of magnetic Tb atoms are related only by the symmetry operations interchanging $\mathbf{k}$ and $-\mathbf{k}$. These symmetry operations are included in the extended little group used in the magnetic superspace groups approach but they are not included in the little group $G_\mathbf{k}$ used in the conventional representation analysis. Refinement of the neutron powder diffraction data obtained at $T = 58$ K revealed that the magnetic structure superspace group is $P112_1/a1'(ab0)0ss$. The refined magnetic structure represents a combination of SDW modulations with a period of $l \sim 32$ Å along the b crystallographic direction combined with very long period SDW modulations ($l \sim 1140$ Å) along the a crystallographic axis propagating over three symmetrically nonequivalent Tb sites.

Further cooling below 58 K results in emergence of the multicomponent magnetic states: (i) a combination of $\mathbf{k}_1$ and $\mathbf{k}_{IC}$ in the temperature range $51 < T < 58$ K; (ii) a mixed magnetic state of $\mathbf{k}_{IC}$, $\mathbf{k}_1$, and $\mathbf{k}_2$ with a partially locked-in incommensurate component in the temperature range $48 < T < 51$ K; and (iii) a pure commensurate multicomponent magnetic state described by a combination of $\mathbf{k}_1$, $\mathbf{k}_2$, $\mathbf{k}_3$, and $\mathbf{k}_4$ below 48 K. Our analysis based on the symmetry considerations and isotropy subgroups approach revealed that the symmetry of the low-temperature magnetic structure can be described by the intersection of two isotropy subgroups associated with irreps of two primary OPs $[\mathbf{k}_2]mD1$ and $[\mathbf{k}_3]mD1$ which give rise to a large magnetic unit cell of $2a \times 12b \times c$ size. The experimentally observed propagation vectors $\mathbf{k}_1$ and $\mathbf{k}_4$ were found to be potentially involved in full description of this magnetic structure as secondary OPs. It can be understood in a way that not all the magnetic distortions within the obtained magnetic unit cell can be described by two primary OPs but the additional distortion modes provided by irreps of the secondary OPs are necessary. Our neutron diffraction data measured on the single-crystal sample in external magnetic fields up to 120 kOe revealed a consistent and simultaneous suppression of all observed antiferromagnetic satellites. This is in agreement with the model of coupled OPs rather than magnetic phase separation.

Such a complex magnetic phase diagram may give rise to the anomaly around $T_t \simeq 50$ K observed on the temperature dependence of the electrical resistivity along the c crystallographic axis. The electrical conductivity of the antiferromagnetically ordered compound can be described as $\sigma_{ij} = 1/\rho_{ij} = \sigma_{ij}^0(1 - \delta)$ [61], where σ_{ij}^0 is the conductivity of the metal with nondeformed Fermi surface, $\delta = \Gamma m$ is proportional to the width of the energy gap at the new zone boundaries, m is normalized magnetization, and Γ depends on the exchange integral between the conduction electrons and localized f electrons. Γ includes the contributions from all new magnetic superzone boundaries cutting the Fermi surface of an antiferromagnetically ordered metal. In the general case, δ is a tensor and can cause an additional contribution to the anisotropy of the resistivity of the antiferromagnetic metal. The change of δ on cooling below the Néel temperature and below temperature of the magnetic phase transition from the

incommensurate magnetic structure to the low-temperature multicomponent magnetic state described by a combination of $\mathbf{k}_1$, $\mathbf{k}_2$, $\mathbf{k}_3$, and $\mathbf{k}_4$ can substantially affect electrical resistivity $\rho(T)$. Application of external magnetic field along the main crystallographic directions triggers metamagnetic phase transitions to the forced ferromagnetic state and changes the value of δ giving rise to the substantial magnetoresistance effect ($\Delta\rho/\rho \approx -54\%$ at $T = 1.5$ K for field along the c axis). The metamagnetic transitions observed below 8 K in a geometry with an external magnetic field applied along the c crystallographic axis and below 3 K in a geometry with a field applied along the b crystallographic axis are of particular interest since they lock the sample into a metastable ferromagnetic state. This transition is accompanied by an irreversible drop of the magnetoresistance $\Delta\rho/\rho$ vs H. The metastable ferromagnetic state is preserved after removing the external field and one has to apply a negative magnetic field to push the sample back to the antiferromagnetic state, as it was evidenced by our magnetization measurements, magnetoresistance data, and neutron diffraction. Appearance of the metastable ferromagnetic state can be ascribed to the presence of a local minimum in the free energy and a low-energy barrier between antiferromagnetic and forced ferromagnetic states. Magnetoelastic interactions along with the strong magnetocrystalline anisotropy and competing exchange interactions seem to be crucial for stabilizing the forced ferromagnetic state after removal of an external magnetic field [62]. It is worth to mention that irreversibilities in the magnetization behavior and the formation of metastable field-induced states were observed in other R_3T-type compounds (Dy_3Co [63], Ho_3Co [27]) as well as in some other highly anisotropic antiferromagnets [64,65].

In summary, we presented a comprehensive study of the magnetic phase diagrams, low-temperature magnetic structures, and field effect on electrotransport properties of the Tb_3Ni single crystal and powder samples. The incommensurate magnetic structure of a SDW type emerging just below Néel temperature has been revealed in Tb_3Ni by the Rietveld refinement of the neutron powder diffraction data using the magnetic superspace groups approach. Low-temperature magnetic structure was found to be commensurate exhibiting large magnetic unit cell $2a \times 12b \times c$ that is described by the irreps of two coupled primary OPs $[\mathbf{k}_2]mD1$ and $[\mathbf{k}_3]mD1$ and involves the irreps of the propagation vectors $\mathbf{k}_1$ and $\mathbf{k}_4$ as secondary OPs. Such a complex magnetic phase diagram gives rise to the anomaly around $T_t \approx 50$ K observed on the temperature dependence of the electrical resistivity along the c crystallographic axis. Particularly, the formation of energy gaps on magnetic superzone boundaries, i.e., the magnetic superzone effect, can provide an additional contribution to the electrical resistivity in the antiferromagnetic systems. Application of an external magnetic field was found to suppress the complex low-temperature antiferromagnetic states in Tb_3Ni and induce metamagnetic transitions to the forced ferromagnetic state that are accompanied by a substantial magnetoresistance effect. The forced ferromagnetic state induced after application of an external magnetic field along the b and c crystallographic axes was found to be irreversible below 3 and 8 K, respectively. The exponential law of the hysteresis loop width $\Delta H(T)$ was observed in an external magnetic field applied along the c axis of the Tb_3Ni single-crystal sample. The magnetic phase diagrams for three different geometries of the single-crystal sample in an external magnetic field have been deduced.

ACKNOWLEDGMENTS

This work was partially supported by FASO Russia (Projects No. AAAA-A18-118020190112-8 and No. AAAA-A18-118020290129-5). This research used resources at the Spallation Neutron Source, a DOE Office of Science User Facility operated by the Oak Ridge National Laboratory. The National High Magnetic Field Laboratory is supported by National Science Foundation Cooperative Agreement No. DMR-1157490 and the state of Florida. This work is partly based on experiments performed at the Swiss spallation neutron source SINQ, Paul Scherrer Institute, Villigen, Switzerland. S.E.N. acknowledges support from the International Max Planck Research School for Chemistry and Physics of Quantum Materials (IMPRS-CPQM).

[1] *Handbook of Ferromagnetic Materials*, edited by K. H. J. Buschow, Vol. 4 (Elsevier, Amsterdam, 1988).

[2] A. K. Pathak, D. Paudyal, Y. Mudryk, and V. K. Pecharsky, Role of $4f$ electrons in crystallographic and magnetic complexity, Phys. Rev. B **96**, 064412 (2017).

[3] I. D. Hughes, M. Dane, A. Ernst, W. Hergert, M. Luders, J. Poulter, J. B. Staunton, A. Svane, Z. Szotek, and W. M. Temmerman, Lanthanide contraction and magnetism in the heavy rare-earth elements, Nature (London) **446**, 650 (2007).

[4] D. S. Inosov, D. V. Evtushinsky, A. Koitzsch, V. B. Zabolotnyy, S. V. Borisenko, A. A. Kordyuk, M. Frontzek, M. Loewenhaupt, W. Löser, I. Mazilu, H. Bitterlich, G. Behr, J.-U. Hoffmann, R. Follath, and B. Büchner, Electronic Structure and Nesting-Driven Enhancement of the RKKY Interaction at the Magnetic Ordering Propagation Vector in Gd_2PdSi_3 and Tb_2PdSi_3, Phys. Rev. Lett. **102**, 046401 (2009).

[5] A. Koitzsch, N. Heming, M. Knupfer, B. Büchner, P. Y. Portnichenko, A. V. Dukhnenko, N. Y. Shitsevalova, V. B. Filipov, L. L. Lev, V. N. Strocov, J. Ollivier, and D. S. Inosov, Nesting-driven multipolar order in CeB_6 from photoemission tomography, Nat. Commun. **7**, 10876 (2016).

[6] N. V. Baranov, A. V. Proshkin, A. F. Gubkin, A. Cervellino, H. Michor, G. Hilscher, E. G. Gerasimov, G. Ehlers, M. Frontzek, and A. Podlesnyak, Enhanced survival of short-range magnetic correlations and frustrated interactions in R_3T intermetallics, J. Magn. Magn. Mater. **324**, 1907 (2012).

[7] N. Sato, K. Imamura, T. Sakon, T. Komatsubara, I. Umehara, and K. Sato, Is La_3Ni a new unconventional superconductor? J. Phys. Soc. Jpn. **63**, 2061 (1994).

[8] T. H. Geballe, B. T. Matthias, V. B. Compton, E. Corenzwit, G. W. Hull, and L. D. Longinotti, Superconductivity in binary alloy systems of the rare earths and of thorium with Pt-group metals, Phys. Rev. **137**, A119 (1965).

[9] A. Podlesnyak, G. Ehlers, H. Cao, M. Matsuda, M. Frontzek, O. Zaharko, V. A. Kazantsev, A. F. Gubkin, and N. V. Baranov, Temperature-driven phase transformation in Y_3Co: Neutron scattering and first-principles studies, Phys. Rev. B **88**, 024117 (2013).

[10] N. V. Baranov, A. A. Yermakov, P. E. Markin, U. M. Possokhov, H. Michor, B. Weingartner, G. Hilscher, and B. Kotur, Magnetic phase transitions, short-range correlations and spin fluctuations in $(Gd_{1-x}Y_x)_3Co$, J. Alloys Compd. **329**, 22 (2001).

[11] N. V. Baranov, E. Bauer, R. Hauser, A. Galatanu, Y. Aoki, and H. Sato, Field-induced phase transitions and giant magnetoresistance in Dy_3Co single crystals, Eur. Phys. J. B **16**, 67 (2000).

[12] A. Podlesnyak, A. Daoud-Aladine, O. Zaharko, P. Markin, and N. Baranov, Magnetic structures and magnetic phase transitions in Ho_3Co, J. Magn. Magn. Mater. **272–276**, 565 (2004).

[13] N. V. Baranov, A. F. Gubkin, A. P. Vokhmyanin, A. N. Pirogov, A. Podlesnyak, L. Keller, N. V. Mushnikov, and M. I. Bartashevich, High-field magnetization and magnetic structure of Tb_3Co, J. Phys.: Condens. Matter **19**, 326213 (2007).

[14] D. Gignoux, J. C. Gomez-Sal, and D. Paccard, Magnetic properties of a Tb_3Ni single crystal, Solid State Commun. **44**, 695 (1982).

[15] A. F. Gubkin, A. Podlesnyak, and N. V. Baranov, Single-crystal neutron diffraction study of the magnetic structure of Er_3Co, Phys. Rev. B **82**, 012403 (2010).

[16] G. J. Primavesi and K. N. R. Taylor, Magnetic transitions in the rare earth intermetallic compounds R_3Ni and R_3Co, J. Phys. F **2**, 761 (1972).

[17] B. Li, J. Du, W. J. Ren, W. J. Hu, Q. Zhang, D. Li, and Z. D. Zhang, Large reversible magnetocaloric effect in Tb_3Co compound, Appl. Phys. Lett. **92**, 242504 (2008).

[18] S. K. Tripathy, K. G. Suresh, and A. K. Nigam, A comparative study of the magnetocaloric effect in Gd_3Co and Gd_3Ni, J. Magn. Magn. Mater. **306**, 24 (2006).

[19] P. Kumar, N. K. Singh, A. K. Nayak, A. Haldar, K. G. Suresh, and A. K. Nigam, Large reversible magnetocaloric effect in Er_3Co compound, J. Appl. Phys. **107**, 09A932 (2010).

[20] J. Shen, J.-L. Zhao, F.-X. Hu, G.-H. Rao, G.-Y. Liu, J.-F. Wu, Y.-X. Li, J.-R. Sun, and B.-G. Shen, Magnetocaloric effect in antiferromagnetic Dy_3Co compound, Appl. Phys. A **99**, 853 (2010).

[21] D. T. Cromer and A. C. Larson, The crystal structure of La_3Co, Acta Crystallogr. **14**, 1226 (1961).

[22] N. V. Baranov, G. Hilscher, A. V. Korolev, P. E. Markin, H. Michor, and A. A. Yermakov, Magnetic, thermal and electrical properties of Er_3Co studied on single crystals, Physica B **324**, 179 (2002).

[23] N. V. Baranov, K. Inoue, H. Michor, G. Hilscher, and A. A. Yermakov, Spin fluctuations in Gd_3Rh induced by f-d exchange: The influence on the T-linear specific heat, J. Phys.: Condens. Matter **15**, 531 (2003).

[24] N. V. Baranov, H. Michor, G. Hilscher, A. Proshkin, and A. Podlesnyak, Extra T-linear specific heat contribution induced by the f-d exchange in Gd-Ni binary compounds, J. Phys.: Condens. Matter **20**, 325233 (2008).

[25] E. Talik, Magnetic and transport properties of the R_3Ni system (R = Y, Gd, Tb, Dy, Ho, Er), Physica B **193**, 213 (1994).

[26] E. Talik and M. Neumann, Spin fluctuations in the R_3T compounds (R = Gd, T = Ir, Rh), J. Magn. Magn. Mater. **140–144**, 795 (1995).

[27] N. V. Baranov, T. Goto, G. Hilscher, P. E. Markin, H. Michor, N. V. Mushnikov, J.-G. Park, and A. A. Yermakov, Irreversible field-induced magnetic phase transitions and properties of Ho_3Co, J. Phys.: Condens. Matter **17**, 3445 (2005).

[28] K. Prokeš and F. Yokoachiya, Helmholtz-Zentrum Berlin für materialien und energie. E4: The 2-axis diffractometer at BER II, J. Large Scale Res. Facil. **3**, A104 (2017).

[29] G. Ehlers, A. Podlesnyak, J. L. Niedziela, E. B. Iverson, and P. E. Sokol, The new cold neutron chopper spectrometer at the spallation neutron source: Design and performance, Rev. Sci. Instrum. **82**, 085108 (2011).

[30] G. Ehlers, A. Podlesnyak, and A. I. Kolesnikov, The cold neutron chopper spectrometer at the Spallation Neutron Source: A review of the first 8 years of operation, Rev. Sci. Instrum. **87**, 093902 (2016).

[31] J. Schefer, P. Fischer, H. Heer, A. Isacson, M. Koch, and R. Thut, A versatile double-axis multicounter neutron powder diffractometer, Nucl. Instrum. Methods Phys. Res. Sect. A **288**, 477 (1990).

[32] V. Petříček, M. Dušek, and L. Palatinus, Crystallographic computing system JANA2006: General features, Z. Kristallogr. Cryst. Mater. **229**, 345 (2014).

[33] A. F. Gubkin, E. A. Sherstobitova, P. B. Terentyev, A. Hoser, and N. V. Baranov, A cluster-glass magnetic state in R_5Pd_2 (R = Ho, Tb) compounds evidenced by ac-susceptibility and neutron scattering measurements, J. Phys.: Condens. Matter **25**, 236003 (2013).

[34] T. Tsutaoka, K. Obata, A. A. Sherstobitov, E. G. Gerasimov, P. B. Terentev, and N. V. Baranov, Magnetic order, phase transitions and electrical resistivity of Ho_7Rh_3 single crystals, J. Alloys Compd. **654**, 126 (2016).

[35] E. Talik, M. Klimczak, R. Troć, J. Kusz, W. Hofmeister, and A. Damm, Comparison of the magnetic properties of Gd_7T_3 (T = Pd and Rh) single crystals, J. Alloys Compd. **427**, 30 (2007).

[36] R. V. Colvin, S. Legvold, and F. H. Spedding, Electrical resistivity of the heavy rare-earth metals, Phys. Rev. **120**, 741 (1960).

[37] K. Prokeš, E. Brück, F. R. de Boer, M. Mihálik, A. Menovsky, P. Burlet, J. M. Mignot, L. Havela, and V. Sechovský, Giant magnetoresistance and magnetic phase diagram of UNiGa, J. Appl. Phys. **79**, 6396 (1996).

[38] B. Frick, J. Schoenes, O. Vogt, and J. W. Allen, Transport studies of Kondo behavior, ferromagnetic and antiferromagnetic order in $U_{1-x}Th_xSb$, Solid State Commun. **42**, 331 (1982).

[39] T. Tsutaoka, T. Matsushita, A. V. Proshkin, E. G. Gerasimov, P. B. Terentev, and N. V. Baranov, Giant magnetoresistance and field-induced magnetic phase transitions in Gd_7Rh_3 studied on single crystals, J. Alloys Compd. **628**, 230 (2015).

[40] V. Pomjakushin, Full propagation-vector star antiferromagnetic order in quantum spin trimer system $Ca_3CuNi_2(PO_4)_4$, J. Phys.: Condens. Matter **26**, 496002 (2014).

[41] D. M. Hatch and H. T. Stokes, Complete listing of order parameters for a crystalline phase transition: A solution to the generalized inverse Landau problem, Phys. Rev. B **65**, 014113 (2001).

[42] B. J. Campbell, H. T. Stokes, D. E. Tanner, and D. M. Hatch, *ISODISPLACE:* A web-based tool for exploring structural distortions, J. Appl. Crystallogr. **39**, 607 (2006).

[43] A. P. Cracknell, B. L. Davies, S. C. Miller, and W. F. Love, *Kronecker Product Tables. Volume 1. General Introduction*

and Tables of Irreducible Representation of Space Groups (IFI/Plenum, New York, 1979).

[44] H. T. Stokes and D. M. Hatch, Coupled order parameters in the Landau theory of phase transitions in solids, Phase Transitions **34**, 53 (1991).

[45] H. T. Stokes and D. M. Hatch, *Isotropy Subgroups of the 230 Crystallographic Space Groups* (World Scientific, Singapore, 1988).

[46] J. Rodríguez-Carvajal, Recent advances in magnetic structure determination by neutron powder diffraction, Physica B **192**, 55 (1993).

[47] A. Janner and T. Janssen, Symmetry of incommensurate crystal phases. I. Commensurate basic structures, Acta Crystallogr. Sect. A **36**, 399 (1980).

[48] V. Petříček, J. Fuksa, and M. Dušek, Magnetic space and superspace groups, representation analysis: Competing or friendly concepts? Acta Crystallogr. Sect. A **66**, 649 (2010).

[49] J. M. Perez-Mato, J. L. Ribeiro, V. Petricek, and M. I. Aroyo, Magnetic superspace groups and symmetry constraints in incommensurate magnetic phases, J. Phys.: Condens. Matter **24**, 163201 (2012).

[50] I. Urcelay-Olabarria, J. M. Perez-Mato, J. L. Ribeiro, J. L. García-Muñoz, E. Ressouche, V. Skumryev, and A. A. Mukhin, Incommensurate magnetic structures of multiferroic $MnWO_4$ studied within the superspace formalism, Phys. Rev. B **87**, 014419 (2013).

[51] T. Tsutaoka, K. Shimomura, N. V. Baranov, A. V. Proshkin, E. G. Gerasimov, and P. B. Terentev, Giant magnetoresistance and field-induced phase transitions in Tb_7Rh_3 single crystal, J. Korean Phys. Soc. **63**, 563 (2013).

[52] T. Egami, Theory of intrinsic magnetic after-effect I. Thermally activated process, Phys. Status Solidi A **19**, 747 (1973).

[53] T. Egami, Theory of intrinsic magnetic after-effect II. Tunnelling process and comparison with experiments, Phys. Status Solidi A **20**, 157 (1973).

[54] H. Oesterreicher, F. T. Parker, and M. Misroch, Analysis of giant intrinsic magnetic hardness in $SmCo_{5-x}Ni_x$, Phys. Rev. B **18**, 480 (1978).

[55] R. Ribas, B. Dieny, B. Barbara, and A. Labrata, The magnetization process and coercivity in random anisotropy systems, J. Phys.: Condens. Matter **7**, 3301 (1995).

[56] F. T. Parker and H. Oesterreicher, Temperature dependence of intrinsic magnetic hardness in some rare-earth pseudobinary compounds and amorphous materials, Phys. Status Solidi A **75**, 273 (1983).

[57] E. Stryjewski and N. Giordano, Metamagnetism, Adv. Phys. **26**, 487 (1977).

[58] *Introduction to Frustrated Magnetism*, edited by C. Lacroix, P. Mendels, and F. MilaSpringer-Verlag, Berlin, 2011).

[59] *Frustrated Spin Systems*, 2nd ed., edited by H. T. Diep (World Scientific, Singapore, 2013).

[60] I. A. Campbell, Indirect exchange for rare earths in metals, J. Phys. F **2**, L47 (1972).

[61] R. J. Elliott and F. A. Wedgwood, Theory of the resistance of the rare earth metals, Proc. Phys. Soc. **81**, 846 (1963).

[62] N. V. Baranov, E. M. Sherokalova, N. V. Selezneva, A. V. Proshkin, A. F. Gubkin, L. Keller, A. S. Volegov, and E. P. Proskurina, Magnetic order, field-induced phase transitions and magnetoresistance in the intercalated compound $Fe_{0.5}TiS_2$, J. Phys.: Condens. Matter **25**, 066004 (2013).

[63] N. V. Baranov, A. N. Pirogov, and A. E. Teplykh, Magnetic state of Dy_3Co, J. Alloys Compd. **226**, 70 (1995).

[64] K. Sengupta and E. V. Sampathkumaran, Field-induced first-order magnetic phase transition in an intermetallic compound Nd_7Rh_3: Evidence for kinetic hindrance, phase coexistence, and percolative electrical conduction, Phys. Rev. B **73**, 020406 (2006).

[65] Y. Numata, K. Inoue, N. Baranov, M. Kurmoo, and K. Kikuchi, Field-induced ferrimagnetic state in a molecule-based magnet consisting of a Co^{II} ion and a chiral triplet bis(nitroxide) radical, J. Am. Chem. Soc. **129**, 9902 (2007).